

AN IMAGE-PLANE ALGORITHM FOR *JWST*'S NON-REDUNDANT APERTURE MASK DATA

ALEXANDRA Z. GREENBAUM¹, LAURENT PUEYO², ANAND SIVARAMAKRISHNAN^{2,4,5}, AND SYLVESTRE LACOUR³

¹ Johns Hopkins University Department of Physics and Astronomy 3400 North Charles, Baltimore, MD 21218

² Space Telescope Science Institute, 3700 San Martin Drive, Baltimore, MD 21218

³ LESIA, CNRS/UMR-8109, Observatoire de Paris, UPMC, Université Paris Diderot 5 place Jules Janssen, 92195 Meudon, France

Received 2013 March 18; accepted 2014 November 8; published 2014 December 22

ABSTRACT

The high angular resolution technique of non-redundant masking (NRM) or aperture masking interferometry (AMI) has yielded images of faint protoplanetary companions of nearby stars from the ground. AMI on *James Webb Space Telescope* (*JWST*)'s Near Infrared Imager and Slitless Spectrograph (NIRISS) has a lower thermal background than ground-based facilities and does not suffer from atmospheric instability. NIRISS AMI images are likely to have 90%–95% Strehl ratio between 2.77 and 4.8 μm . In this paper we quantify factors that limit the raw point source contrast of *JWST* NRM. We develop an analytic model of the NRM point spread function which includes different optical path delays (pistons) between mask holes and fit the model parameters with image plane data. It enables a straightforward way to exclude bad pixels, is suited to limited fields of view, and can incorporate effects such as intra-pixel sensitivity variations. We simulate various sources of noise to estimate their effect on the standard deviation of closure phase, σ_{CP} (a proxy for binary point source contrast). If $\sigma_{\text{CP}} < 10^{-4}$ radians—a contrast ratio of 10 mag—young accreting gas giant planets (e.g., in the nearby Taurus star-forming region) could be imaged with *JWST* NIRISS. We show the feasibility of using NIRISS' NRM with the sub-Nyquist sampled F277W, which would enable some exoplanet chemistry characterization. In the presence of small piston errors, the dominant sources of closure phase error (depending on pixel sampling, and filter bandwidth) are flat field errors and unmodeled variations in intra-pixel sensitivity. The in-flight stability of NIRISS will determine how well these errors can be calibrated by observing a point source. Our results help develop efficient observing strategies for space-based NRM.

Key words: instrumentation: interferometers – planetary systems – space vehicles: instruments – techniques: high angular resolution

1. INTRODUCTION

Recent direct detections of exoplanets open a spectroscopic window into the atmosphere and physics of young and adolescent exoplanets. They are an important component for piecing together a complete picture of exoplanetary formation and evolution, and are complementary to indirect detections methods. Young and nearby stars have already been surveyed from a few Astronomical Units of physical separation outwards with direct imaging and coronagraphs on eight meter class telescopes (Wahhaj et al. 2013; Nielsen et al. 2013; Biller et al. 2013; Vigan et al. 2012) and are being surveyed at even higher contrast with current (Oppenheimer et al. 2012; Macintosh et al. 2012; Beuzit et al. 2008; Martinache & Guyon 2009) instrument surveys utilizing extreme adaptive optics (ExAO). However, the close environs of young systems in stellar formation regions are only accessible to ExAO systems using interferometric techniques such as non-redundant mask (NRM) interferometry (Lacour et al. 2011; Kraus & Ireland 2012; Cieza et al. 2013; Huélamo et al. 2011). NRM imaging is fundamentally limited by photon noise, so it yields moderate contrast. By comparison, coronagraphs (which suppress light from the bright central object) are capable of delivering higher contrast than NRM, but their search area does not reach as close in as that of NRM. The two techniques are complementary.

NRM was first used to improve the angular resolution of filled-aperture telescopes (Baldwin et al. 1986; Haniff et al.

1987; Tuthill et al. 2000). Its improved dynamic range helped to probe the physics of binaries at moderate contrast ratios (Lloyd et al. 2006; Ireland et al. 2008; Bernat et al. 2010; Martinache et al. 2007, 2009). More recently, NRM observations of star forming regions have discovered structures associated with the birth of exoplanets (Kraus & Ireland 2012; Cieza et al. 2013; Huélamo et al. 2011). Routine ground contrast ratio limits for NRM are 10^2 – 10^3 with the deepest contrast being $\Delta L' = 7.99$ (Hinkley et al. 2011). Today instruments combine NRM with ExAO systems (Sivaramakrishnan et al. 2010b; Zimmerman 2011; Zimmerman et al. 2012). These facilities, together with wide bandpass polarization or integral field unit spectroscopy (IFS) in the *YJHK* bands on the 8 m Gemini South telescope (Macintosh et al. 2014) as well as 2.5–5 μm NRM on the 40K *James Webb Space Telescope*'s Near Infrared Imager and Slitless Spectrograph (*JWST* NIRISS; Doyon et al. 2012; Sivaramakrishnan et al. 2010b, 2012; Greenbaum et al. 2013a), promise to extend planet formation science by enabling deeper dust penetration at longer wavelengths. These new systems will enable detection of very young (e.g., Taurus–Auriga star forming region), possibly accreting gas giant planets at small separations accessible to NIRISS NRM (Beichman et al. 2010).

In spite of the wealth of recent observational results from NRM, the literature does not include extensive discussion of the fundamental and practical limits associated with the technique. Lacour et al. (2011) discussed empirical sensitivity limits of Very Large Telescope (VLT) NACO Sparse Aperture Masking (SAM), based on experiments with the image plane fitting routine that we study here. Martinache (2010) showed how NRM can be generalized to full aperture imaging in the high Strehl ratio regime. Ireland (2013) discussed some of the

⁴ Astrophysics Department, American Museum of Natural History, 79th Street and Central Park West, New York, NY 10024, USA.

⁵ Department of Physics and Astronomy, Stony Brook University, Stony Brook, NY 11794, USA.

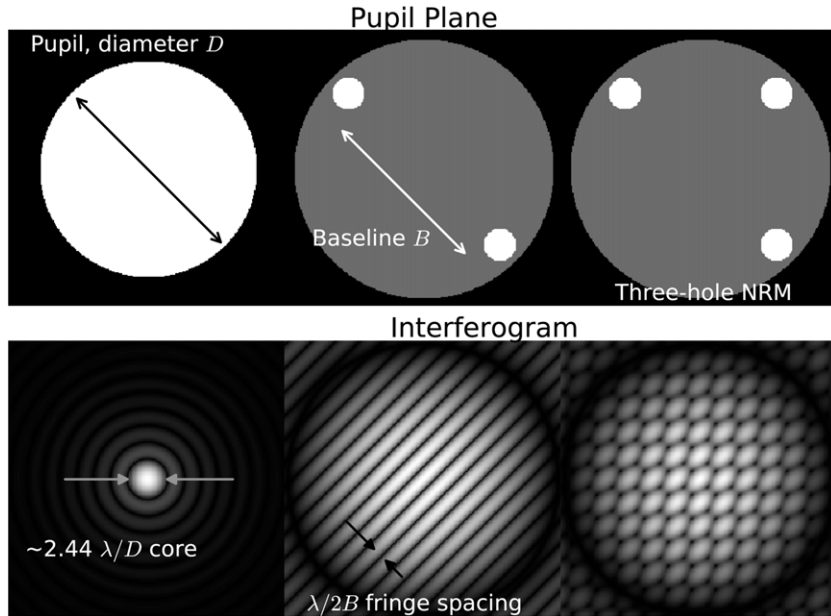


Figure 1. Pupil masks and their interferograms. Small holes produce a large PSF envelope, fringed by interference through multiple holes. The longest baselines provides finer resolution than a full aperture. The three hole pupil at right can provide a *closure phase* measurement of a celestial object.

limiting factors of high contrast NRM observations, and Hinkley et al. (2011) conducted deep NRM observations of the known multiple planetary system HR 8799.

The purpose of this paper is two-fold. First, we continue the development of the image plane approach to analyzing NRM data. We address field of view, pixel sampling, plate scale and pupil magnification stability, and some detector properties. We show that this method typically confirms the photon noise and flat field accuracy limits presented by Ireland (2013). In addition, we study other factors that limit NRM contrast—requirements on the spectral type match between a target and its calibrator star, and the effect a finite spectral bandpass has on closure phase errors. Second, we highlight factors that limit *JWST* NIRISS NRM, which fields a seven-hole NRM (Sivaramakrishnan et al. 2012). NIRISS has the best pupil image quality of all the *JWST* instruments (Bos et al. 2008), which makes it *JWST*'s best-suited instrument for aperture masking interferometry. In addition, NIRISS's homogenous aluminum bench and optics should help achieve uniform contraction of mechanical and optical surfaces as the instrument cools to its operating temperature of about 40 K. NIRISS's all-reflective design philosophy also mitigates against chromatic effects, which can be exacerbated by cryogenic conditions. Finally, some relevant properties of NIRISS NRM are described in the [Appendix](#).

2. BACKGROUND

(Figure 2) A non-redundant mask is a pupil plane mask typically located at a re-imaged pupil plane. It possesses several usually identical holes arranged so that no two hole-to-hole vectors are repeated (thus providing a non-redundant set of *baselines* in the pupil). If its holes are circular, with diameter d when projected back to the primary mirror, at a wavelength λ its point-spread function (PSF) or *interferogram* is contained in an Airy pattern envelope with a first dark ring of diameter $2.44 \lambda/d$ (Figure 1). This envelope is modulated by fringes with half period $\theta = \lambda/2B$ for each baseline. Here B is the hole

separation. Figure 2 shows the *JWST* NIRISS mask with seven hexagonal holes, and its PSF.

The Fourier transform of the detected in-focus two-dimensional image intensity array is the array of *complex visibility*, \mathcal{V} . Because of the baselines' non-redundancy, the fringe amplitude and phase for each baseline or “two hole interferometer” component in the NRM can be measured unambiguously. The array of complex visibilities for a point source through unaberrated optics is the autocorrelation of the pupil mask. The resulting array of complex visibilities form localized *splodges* (Lloyd et al. 2006) of signal in the transform domain—conceptually one independent splodge (or a splodge and its dependent, Hermitian “mirror splodge”) per baseline. Numerical Fourier data analysis approaches measure fringe phases and fringe amplitudes, often at the peak of each splodge amplitude (Tuthill et al. 2000; Lloyd et al. 2006). When using a finite bandwidth filter, selecting a single amplitude and phase to characterize a polychromatic fringe implicitly averages over the bandpass. Furthermore, since windowing in the image plane leads to convolution in the Fourier domain, this induces a second form of averaging within a splodge. Our image plane approach avoids this second form of averaging, but it does perform a conceptually similar averaging over the bandpass. In the absence of wavefront aberration, fringe phases for an on-axis point source are zero. Information on source structure is contained in the fringes that are extracted from the image.

The non-redundancy of baselines in the pupil leads to constraints on the complex fringe visibilities. A *closure phase* (the cyclic sum of fringe phases around the baselines formed by three holes (top right, Figure 1)) is insensitive to constant wavefront delays (pistons) over the holes. The fringe formed by interference of holes i and j has a fringe phase $\phi_{i,j}$ which is proportional to the wavefront delay between holes $\phi_{i,j} \equiv \phi_j - \phi_i$. For a point source (in the absence of higher order aberrations) (e.g., Readhead et al. 1988):

$$\begin{aligned} \Delta\phi_{1,2} + \Delta\phi_{2,3} + \Delta\phi_{3,1} \\ = (\phi_1 - \phi_2) + (\phi_2 - \phi_3) + (\phi_3 - \phi_1) = 0. \end{aligned} \quad (1)$$

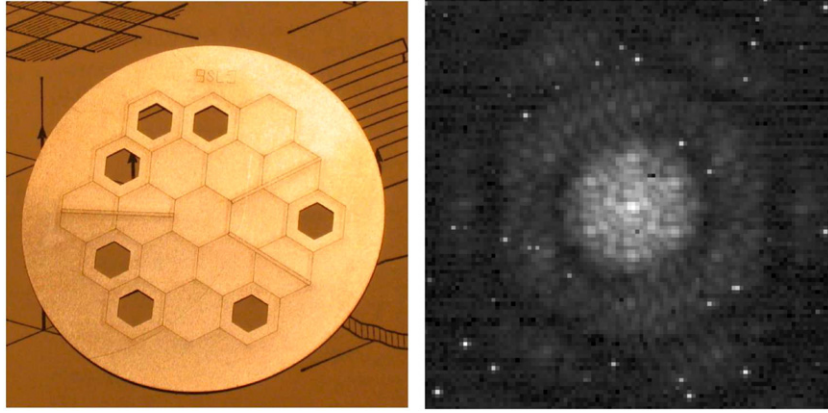


Figure 2. Non-redundant mask for *JWST*’s NIRISS pupil wheel (Sivaramakrishnan et al. 2010a) and its PSF (or interferogram) with NIRISS F430M from cryogenic vacuum tests in 2013 November (Greenbaum et al. 2014). The interferogram’s fine structure is due to the 21 baselines generated by the 7 holes. The PSF envelope reflects the hexagonal hole shape.

Full-aperture images do not yield closure phases, but sufficiently high Strehl ratio images possess certain constrained linear combinations of phases of the Fourier transform of the image (Martinache 2010, 2011). These combinations, or *kernel phases*, are useful for model fitting data when wavefront aberrations are below ~ 1 rad (Martinache 2010; Ireland 2013; Pope et al. 2013).

An N -hole mask has $N(N-1)/2$ baselines, $N(N-1)(N-2)/6$ closure phases, and $(N-1)(N-2)/2$ independent closure phases. Empirically, achievable dynamic range is approximately the inverse of the standard deviation of closure phase error, $1/\sigma_{CP}$ (Lacour et al. 2011).

Closure phases of centro-symmetric sky brightness distributions are zero. Binary or multiple point source models are fit to closure phase data to provide information on structure as fine as $\lambda/2B$. Instrumental contributions to closure phases are measured (in principle) by observing a point source. These contributions are then subtracted from a target’s closure phases. Instrument stability between target and calibrator leads to improved NRM performance. In addition to fringe phases, a space telescope is likely to provide stable fringe amplitudes. Closure amplitudes (a ratio of amplitudes of fringes formed by four holes (Thompson et al. 1986)) are useful in simple model fitting using space-based NRM data, thereby extending NRM model fitting to include centro-symmetric structure such as circular disks. However, Ford et al. (2014) use simulated noisy NIRISS NRM data to extract the fringe amplitudes and phases which they then use to recreate the input target scene with interferometric resolution. They found that enforcing closure quantities on image plane data leads to an increase in spurious image artifacts.

Currently numerical Fourier methods are the most common approach to NRM data analysis (e.g., Monnier 2003; Tuthill et al. 2000; Kraus & Ireland 2012; Ireland et al. 2008). This is suited to fields of view that encompass the first few Airy rings of the NRM PSF’s “primary beam” (the diffraction pattern of a single hole), and pixel scales that are significantly finer than $\lambda/2D$. Palomar Hale’s PHARO, Keck-NIRC2, and VLT’s NACO all possess 3-5 pixels per resolution element (Metchev & Hillenbrand 2004; Ireland et al. 2011; Tuthill et al. 2000; Girard 2013). With such super-Nyquist fine pixellation, Fourier methods easily identify and interpolate over isolated bad pixels (Ireland 2013).

Diffraction-limited exoplanet imagers deploying state-of-the-art ExAO systems now feed IFs (Oppenheimer et al. 2012; Macintosh et al. 2014; Beuzit et al. 2008). These imaging

spectrographs typically have limited fields of view since several detector pixels are required for each image plane pixel spectrum, and the angular extent of each image plane lenslet is at or below the diffraction limit of the telescope, so the instruments are often limited by the number of available detector pixels. NRM on these hyperspectral imagers—Palomar’s P1640 (Zimmerman 2011; Zimmerman et al. 2012) and Gemini Planet Imager (Sivaramakrishnan et al. 2010b; Greenbaum et al. 2013b)—must deal with this limitation. An image plane based approach (e.g., Lacour et al. 2011; Cheetham et al. 2012; Greenbaum et al. 2013a) is insensitive to these restrictions on the field of view.

Future space-based NRM on *JWST* NIRISS (e.g., Sivaramakrishnan et al. 2009a, 2009b, 2010a, 2012; Greenbaum et al. 2013a) is implemented on coarse pixel scales. Under these conditions a numerical Fourier data reduction approach may require more data in order to reduce contamination by bad pixels. This is more relevant to coarse—barely or sub-Nyquist—pixel scales. Dithering to fill the image plane pixels with valid data decreases observing efficiency and complicates estimates of noise. An image plane based approach sidesteps the requirement of knowing every pixel value in the image. The image plane approach is also robust to detector non-linearities that may occur at the centers of NRM images, since suspect pixel data can be discarded. *JWST* NIRISS’s coarse pixel scales also increase its sensitivity to non-uniform sensitivity within a pixel (intra-pixel sensitivity, or IPS), and pixel-to-pixel variations in IPS (Hardy et al. 2008). Image plane data reduction can take IPS into account, with a map of measured variations or a model of the pixel sensitivities (Greenbaum et al. 2013a).

3. IMAGE PLANE MODELING

We assume the image plane complex amplitude induced by a point source at infinity is described by the Fourier transform of the aperture transmission function (i.e., the Fraunhofer approximation). If functions F and f are a Fourier transform pair, we write $F \stackrel{F.T.}{\rightleftharpoons} f$. We develop a polychromatic image plane model tailored to *JWST* NIRISS’s seven hole NRM (Figure 2). Each hole is a hexagon, which, when projected to the *JWST* primary mirror, has a flat-to-flat distance of approximately 0.8 m. Our model can be adapted to arbitrary hole locations and polygonal hole shapes (e.g., Greenbaum et al. 2013b). Here we treat circular holes with diameter d or hexagonal holes with flat-to-flat distance D (Figure 3), utilizing a closed form for

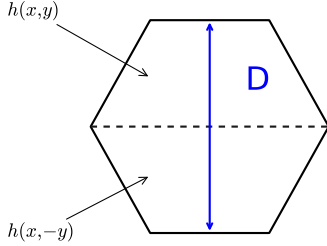


Figure 3. In Sabatke et al. (2005) D is the flat-to-flat distance. The hexagon is split into two symmetric parts, $a_{\text{hex}}(x, y)$ and $a_{\text{hex}}(x, -y)$, whose transforms, $g(k_x, k_y)$ and $g(k_x, -k_y)$ are computed analytically (Equation (6)).

the Fourier transform of a hexagon (Sabatke et al. 2005), while noting that other more specialized derivations for this exist in the literature (Troy & Chanan 2003). We extend the work of Sabatke et al. (2005) to include limiting values for the analytical expression's three singular lines and singular central point.

We calculate the monochromatic NRM PSF at a wavelength λ analytically, and construct polychromatic PSFs by summing appropriately weighted monochromatic PSFs on a finely sampled numerical grid. We then bin this finely sampled image to the detector pixel scale to simulate a pixelated noiseless NRM PSF.

We denote the pupil transmission function by $A(\mathbf{x})$. A hole with a transmission function $A_h(\mathbf{x})$ produces an image plane complex amplitude $a_h(\mathbf{k})$ (where $a_h \stackrel{F.T.}{\rightleftharpoons} A_h$) and a PSF $P = a_h a_h^*$ (where $*$ indicates complex conjugation). If the pupil plane vector $\mathbf{x} = (x, y)$ is in units of the wavelength of the monochromatic light, the image plane (or spatial frequency) vector $\mathbf{k} = (k_x, k_y)$ is in cycles across the pupil. $P(\mathbf{k})$ is the *primary beam*, by analogy with radio interferometry, and is the envelope of the NRM PSF. Vector baselines create the finer scale fringing in the NRM PSF.

3.1. Circular Mask Holes

A circular aperture's transmission function is

$${}^2\Pi(\mathbf{x}) = \begin{cases} 1, & r < \frac{1}{2} \\ 0, & r \geq \frac{1}{2} \end{cases}, \quad (2)$$

where $r = \sqrt{x^2 + y^2}$. The transmission function of a mask with N identical circular holes centered at $\{\mathbf{x}_i, i = 1, \dots, N\}$ is

$$A(\mathbf{x}) = \sum_{i=1}^N {}^2\Pi\left(\frac{\mathbf{x} - \mathbf{x}_i}{d_\lambda}\right), \quad (3)$$

(where $d_\lambda \equiv d/\lambda$). The image plane complex amplitude of an on-axis monochromatic point source observed through this mask is

$$a(\mathbf{k}) \stackrel{F.T.}{\rightleftharpoons} A(\mathbf{x}). \quad (4)$$

Following the nomenclature of phase retrieval work on the Hubble Space Telescope, we call $a(\mathbf{k})$ the *amplitude spread function* (ASF).

Invoking Fourier shift and scaling theorems,

$${}^2\Pi\left(\frac{\mathbf{x} - \mathbf{x}_0}{d_\lambda}\right) \stackrel{F.T.}{\rightleftharpoons} (d_\lambda)^2 \text{Jinc}(kd_\lambda) e^{-i\mathbf{k}\cdot\mathbf{x}_0}, \quad (5)$$

where $\text{Jinc}(k) \equiv J_1(\pi k)/2k$ is the transform of the circular transmission function. Here J_1 is the Bessel function of the first kind, of order 1. The phase gradient term $e^{-i\mathbf{k}\cdot\mathbf{x}_0}$ reflects the shift of the hole's origin to \mathbf{x}_0 .

3.2. Hexagonal Mask Holes

We denote the hexagonal hole Fourier transform by $a_{\text{hex}}(\mathbf{k})$. Following Sabatke et al. (2005), $g(k_x, k_y)$ is the Fourier transform of one half of a hexagon that is bisected from one corner to its diametrically opposite corner (Figure 3):

$$\begin{aligned} g(k_x, k_y) &= \frac{\exp\left[-i\pi D \left(\frac{2k_x}{\sqrt{3}} + k_y\right)\right]}{4\pi^2(k_x^3 - 3k_x k_y^3)} (\sqrt{3}k_x - 3k_y) \\ &\times \left(\left\{ \exp(i\pi D \sqrt{3}k_x) - \exp\left[i\pi D \left(\frac{4}{\sqrt{3}}k_x + k_y\right)\right] \right\} \right. \\ &\left. + (\sqrt{3}k_x + 3k_y) [\exp(i\pi D k_x/\sqrt{3}) - \exp(i\pi D k_y)] \right) \\ a_{\text{hex}}(k_y, k_x) &= g(k_x, k_y) + g(k_x, -k_y). \end{aligned} \quad (6)$$

The function g has numerical singularities along three lines, $k_x = 0$ and $k_x = \pm\sqrt{3}k_y$. The limiting behavior along $k_x = 0$ and at the origin is

$$\begin{aligned} g(0, k_y) &= \frac{e^{-iD\pi k_y}}{2\sqrt{3}\pi^2 k_y^2} \\ &\times (-1 + iD\pi k_y + e^{iD\pi k_y} - 2iD\pi k_y e^{iD\pi k_y}) \end{aligned} \quad (7)$$

$$g(0, 0) = \frac{\sqrt{3}D^2}{4}. \quad (8)$$

Values along the other two lines can be found by invoking symmetry arguments, and replacement with the appropriate limiting value taken from the $k_x = 0$ line.

3.3. Interference between Holes

In the absence of wavefront error the ASF of a mask with N identical holes centered at $\{\mathbf{x}_i, i = 1, \dots, N\}$ is

$$\sum_{i=1}^N A(\mathbf{x} - \mathbf{x}_i) \stackrel{F.T.}{\rightleftharpoons} a(\mathbf{k}) = a_h(\mathbf{k}) \sum_{i=1}^N e^{-i\mathbf{k}\cdot\mathbf{x}_i} \quad (9)$$

($a_h(\mathbf{k})$ is a single hole ASF). The mask's point spread function is

$$p(\mathbf{k}) = a(\mathbf{k})a^*(\mathbf{k}) = P(\mathbf{k}) \sum_{i=1}^N \sum_{j=1}^N e^{-i\mathbf{k}\cdot(\mathbf{x}_i - \mathbf{x}_j)} \quad (10)$$

or

$$\begin{aligned} p(\mathbf{k}) &= P(\mathbf{k}) \{ N + e^{-i\mathbf{k}\cdot(\mathbf{x}_1 - \mathbf{x}_2)} + e^{i\mathbf{k}\cdot(\mathbf{x}_1 - \mathbf{x}_2)} \\ &\quad + e^{-i\mathbf{k}\cdot(\mathbf{x}_1 - \mathbf{x}_3)} + e^{i\mathbf{k}\cdot(\mathbf{x}_1 - \mathbf{x}_3)} + \dots \}, \end{aligned}$$

(which is real and nonnegative for any \mathbf{k}). The flux in this image is the two-dimensional integral $\int NP(\mathbf{k})d\mathbf{k}$, taken over

the entire \mathbf{k} plane. We rewrite the PSF as

$$p(\mathbf{k}) = P(\mathbf{k}) \left\{ N + \sum_{i < j} 2 \cos(\mathbf{k} \cdot (\mathbf{x}_i - \mathbf{x}_j)) \right\}, \quad (11)$$

which shows the separate roles the vector baselines and the primary beam play in the morphology of a point source's interferogram.

Wavefront errors $\{\phi_i, i = 1, \dots, N\}$ that are constant within each of the apertures decenter each fringe by $(\phi_i - \phi_j)$. Such errors are termed *pistons*. Pistons do not move the image centroid, since the intensity centroid is the mean of the phase gradient over the (uniformly illuminated) pupil forming an in-focus image (Teague 1982), and piston errors do not change the mean wavefront slope. A piston difference between two holes shifts the fringe away from the image centroid (or *pointing center*) by an angle, the *fringe phase*. A shift from one fringe maximum to the next is interpreted as an angle of 2π . Given *JWST* NIRISS' anticipated image quality during normal operations, we expect fringe phases of point source NRM images to lie well inside the half-open interval $(-\pi, \pi]$. This removes any technical difficulties associated with a fringe phase wrapping around 2π . We stress that fringe phases are not the argument of a "phasor" associated with the complex amplitude of an electromagnetic wave. The expression for the interferometric PSF in the presence of only piston errors is

$$\begin{aligned} p(\mathbf{k}) &= P(\mathbf{k}) \sum_{i=1}^N \sum_{j=1}^N e^{-i\mathbf{k} \cdot (\mathbf{x}_i - \mathbf{x}_j) + i(\phi_i - \phi_j)} \\ &= P(\mathbf{k}) \left\{ N + \sum_{i < j} 2 \cos(\mathbf{k} \cdot (\mathbf{x}_i - \mathbf{x}_j) + (\phi_i - \phi_j)) \right\} \\ &= P(\mathbf{k}) \left\{ N + \sum_{i < j} 2(\cos(\mathbf{k} \cdot (\mathbf{x}_i - \mathbf{x}_j)) \cos(\phi_i - \phi_j) \right. \\ &\quad \left. - \sin(\mathbf{k} \cdot (\mathbf{x}_i - \mathbf{x}_j)) \sin(\phi_i - \phi_j)) \right\}. \quad (12) \end{aligned}$$

3.4. The *JWST* NRM PSF

For *JWST* NIRISS's 7-hole hexagonal mask, Equation (12) gives

$$\begin{aligned} p(\mathbf{k}) &= P(\mathbf{k}) \{ 7 + 2 \cos(\mathbf{k} \cdot (\mathbf{x}_1 - \mathbf{x}_2)) \cos(\Delta\phi_{1,2}) \\ &\quad - 2 \sin(\mathbf{k} \cdot (\mathbf{x}_1 - \mathbf{x}_2)) \sin(\Delta\phi_{1,2}) \\ &\quad + 2 \cos(\mathbf{k} \cdot (\mathbf{x}_1 - \mathbf{x}_3)) \cos(\Delta\phi_{1,3}) \\ &\quad - 2 \sin(\mathbf{k} \cdot (\mathbf{x}_1 - \mathbf{x}_3)) \sin(\Delta\phi_{1,3}) + \dots \}. \quad (13) \end{aligned}$$

With this closed form rapid calculation of monochromatic and polychromatic PSFs on a fine scale is straightforward.

3.5. Linear Fit

Piston differences enter into Equation (13) as coefficients of the sines and cosines describing the baselines' fringes. NIRISS's seven-hole mask has 42 such fringe coefficients— $\cos \Delta\phi_{i,j}$'s and $\sin \Delta\phi_{i,j}$'s, which we rename a_{ij} 's and b_{ij} 's, respectively. Two additional parameters are required to match the model to data: the average flux per hole, F , and a DC offset C :

$$\begin{aligned} F P(\mathbf{k}) &\left\{ N + \sum_{i < j} 2[\cos(\mathbf{k} \cdot (\mathbf{x}_i - \mathbf{x}_j)) \cos(\Delta\phi_{i,j}) \right. \\ &\quad \left. - \sin(\mathbf{k} \cdot (\mathbf{x}_i - \mathbf{x}_j)) \sin(\Delta\phi_{i,j})] \right\} + C. \quad (14) \end{aligned}$$

These 44 parameters can be estimated from image plane pixel data by using an unweighted *linear* least squares minimization of the quantity

$$||\text{data} - \text{model}(a_{ij}, b_{ij}, F, C)||$$

and performing a matrix inversion to recover the parameters. We did not detect significant improvement of a noise-weighted fit over an equally weighted fit, so we use the latter. The piston differences, or fringe phases, are found with

$$\Delta\phi_{ij} = \arctan(b_{ij}/a_{ij}). \quad (15)$$

For uniformly transmissive optics throughput, no scattered light, no significant high spatial frequency wavefront errors, and perfect detectors we expect the trigonometric identity

$$b_{ij}^2 + a_{ij}^2 = 1$$

to hold when imaging a point source. Model parameters derived from fitting real data rarely obey this identity. Instead, we obtain the square of the ij^{th} fringe visibility:

$$b_{ij}^2 + a_{ij}^2 = \mathcal{V}_{ij} \mathcal{V}_{ij}^*. \quad (16)$$

Target structure further reduces fringe visibility. We calculate fringe visibilities in our simulated data sets by measuring coefficients $\{a_{ij}, b_{ij}\}$. We calculate all 35 possible closure phases in NIRISS's seven-hole NRM. Only 15 of these are independent measurements.

We evaluate our model PSF on a 3×3 sub-pixel grid (unless otherwise noted) so we can study sub-pixel effects, and then bin the array to the detector pixel scale. A full pupil distortion model was not used in this study, although real data will require detailed knowledge of the NRM-to-primary mapping.

A polychromatic model is generated with an appropriately weighted sum of each monochromatic fringe model, given the bandpass profile:

$$\begin{aligned} \text{model} &= \sum_{\lambda} F_{\lambda} P(\mathbf{k}_{\lambda}) \\ &\times \left\{ N + \sum_{i < j} 2[\cos(\mathbf{k}_{\lambda} \cdot (\mathbf{x}_i - \mathbf{x}_j)) \cos(\Delta\phi_{i,j}) \right. \\ &\quad \left. - \sin(\mathbf{k}_{\lambda} \cdot (\mathbf{x}_i - \mathbf{x}_j)) \sin(\Delta\phi_{i,j})] \right\}. \quad (17) \end{aligned}$$

In the presence of non-zero piston error the model in Equation (14) does not fit polychromatic data perfectly, because piston error scales inversely with wavelength. This means that the fringes' coefficients, $\cos(\Delta\phi_{i,j})$ and $\sin(\Delta\phi_{i,j})$, themselves vary with wavelength, but our fit keeps these coefficients constant over the bandpass. The narrower the fractional bandwidth of the filter, the smaller the variation of these coefficients. This problem is common to both the image plane as well as the numerical Fourier approach to NRM data analysis. The least squares solution (Equations (15) and (16)) produces an estimate of fringe phase and amplitude that describes some average over the bandpass. We use this estimate in our polychromatic studies.

3.6. Applicability of the Model

NRM is suited to wavefronts that are smooth over each hole in the mask. Our model assumes flat wavefronts over each hole,

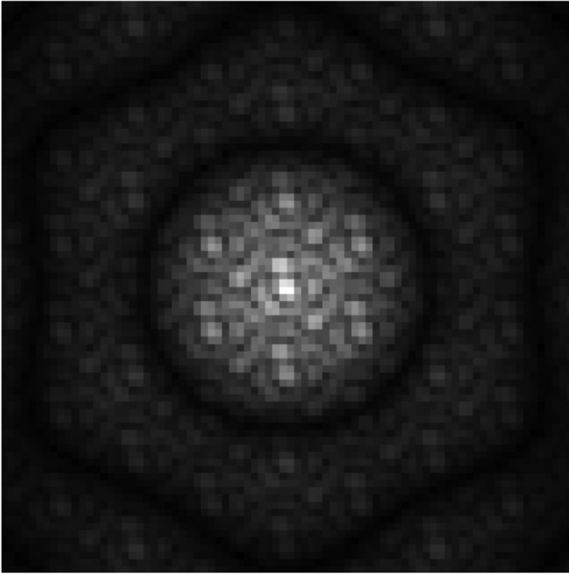


Figure 4. Asserting the static pistons from Table 2 in this simulated PSF produce asymmetric features.

Filter	λ_C (μm)	$\delta\lambda/\lambda$	$\lambda/2D$ (mas)
F480M	4.8	0.08	76
F430M	4.3	0.05	68
F380M	3.8	0.05	60
F277W	2.7	0.25	44

Notes. λ_C is the filter central wavelength, and $\delta\lambda$ is the half-power width of the filter. The Nyquist pixel scale $\lambda/2D$ uses the nominal equivalent area *JWST* mirror diameter $D = 6.5$. NIRISS’s pixel scale is 65 mas.

which averages over fine wavefront structure in some manner. A Fourier approach windows image data, which also averages phase and visibility information (since image plane windowing is a convolution in the Fourier domain). However, the two approaches propagate image plane noise differently. We discuss the effects of high spatial frequency wavefront error in Section 6.

Table 1 describes NIRISS NRM filters relevant to exoplanet studies. We study filter bandpass, source temperature, and spectral type effects using our polychromatic PSF model. When using F277W and F380M, NIRISS’ 65 mas square detector pixels are coarser than Nyquist-sampled.

4. PHOTON NOISE, FLAT FIELD ERROR, AND INTRA-PIXEL SENSITIVITY

We inserted piston wavefront errors over the holes (Table 2 and Figure 4) to examine their effects on simulated monochromatic images. Our pistons are all smaller than $\lambda/4$, which avoids phase wrapping.

We generate monochromatic $4.3\ \mu\text{m}$ images either 3 or 5 times finer than the NIRISS pixel scale prior to binning to its detector scale and performing a least squares determination of the 44 model parameters. We measure closure phase standard deviation for different noise parameters for a set of 15 independent closure triangles (Figure 5). In the absence of added noise our measured closure phases were numerically indistinguishable from zero.

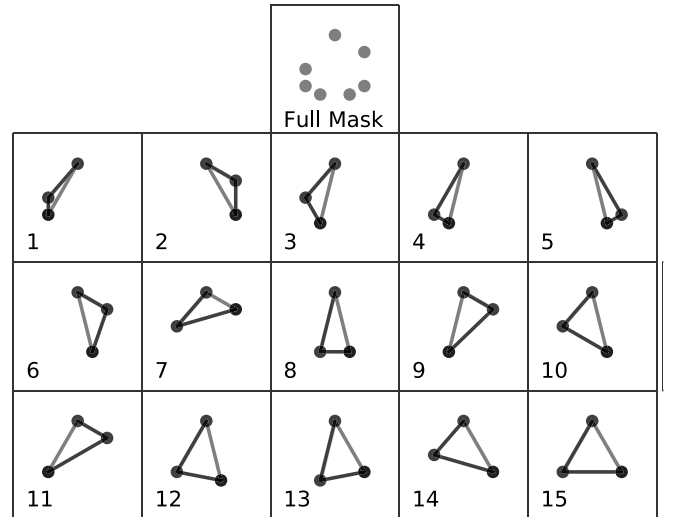


Figure 5. Closure triangles: the set of 15 independent closure triangles corresponding to the figures in Sections 4–6, ordered by increasing perimeter.

Piston in Waves at $4.3\ \mu\text{m}$
+0.02884
−0.06150
+0.12400
−0.02040
+0.01660
−0.03960
−0.04780

Notes. Our simulations use a set of uniformly distributed, random static pistons with a mean of zero and standard deviation 0.06 waves. Anticipated *JWST* NIRISS rms wavefront error at $4.3\ \mu\text{m}$ is approximately $\lambda/30$.

We find that the quality of the fit does not change significantly with field of view (i.e., the number of pixels used). We used data within the first dark Airy ring of the primary beam in all simulations.

We distinguish between two types of closure triangle response to different sources of noise or error.

1. *Baseline-independent* behavior limits contrast at all spatial frequencies similarly.
2. *Baseline-dependent* behavior varies with baseline length and therefore closure triangle. This behavior preferentially limits contrast at higher frequencies, or smaller angular resolution.

4.1. Photon Noise

We investigate a range of exposures, from 10^4 to 10^{11} photoelectron counts (assuming coadding of multiple exposures regardless of pixel well depth). We calculate the standard deviation of each of the 35 closure phases over 25 independent realizations, and plot the mean of these standard deviations, σ_{CP} , as the solid line in Figure 6. Our results are consistent with the

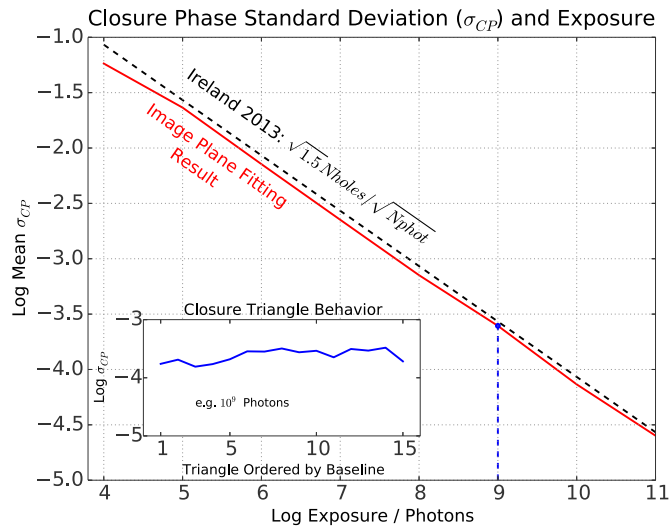


Figure 6. Exposure time (monochromatic): the mean closure phase standard deviation for a range of exposure. The solid red line shows our simulation results; the dotted black line displays the noise limit of Ireland (2013). The inset shows one example of σ_{CP} for each of the 15 triangles in Figure 5 for an exposure with 10^9 photons. Photon noise induces *baseline-independent* errors.

Ireland (2013) result

$$\sigma_{CP} = \sqrt{1.5} \frac{N_{holes}}{\sqrt{N_{phot}}}$$

indicated by the dotted line. The inset plot in Figure 6 displays the behavior of the closure phases plotted in order of increasing closure triangle perimeter. Photon noise contributes *baseline-independent* error.

4.2. Flat Field Error

We simulated multiplicative flat field error with an arrays of uncorrelated pixel-to-pixel noise drawn from a Gaussian distribution. The standard deviation of the Gaussian distributions range from 0.03% to 3%. Figure 7 shows our simulation alongside the Ireland (2013) result:

$$\sigma_{CP} \lesssim 0.3\sigma_{FF}.$$

The small offset between the two results may be a difference in number of pixels used or in the way error is modeled. Both results show the same trend. Flat field error is a *baseline-independent* effect.

4.3. Pixel-to-pixel Variations in Intra-pixel Sensitivity

We use a data-based model of the NIRISS detector’s intra-pixel sensitivity (Hardy et al. 2008). The pixel has maximum sensitivity at its center, but the sensitivity drops smoothly to $80\% \pm 5\%$ of its peak at the pixel corners (Figure 8(B)–left). We implement a parabolic drop-off of sensitivity within a pixel.

Lauer (1999) describes a single image (integrated over each pixel) on a detector as

$$I(x, y) = O(x, y) * P(x, y)(\text{III}(x, y) * \mathfrak{R}(x, y)), \quad (18)$$

where the image is a convolution of the object, $O(x, y)$ and the PSF $P(x, y)$ multiplied by a sampling function convolved with the intra-pixel response, $\mathfrak{R}(x, y)$. If $\mathfrak{R}(x, y)$ is symmetric it will not contribute phase to the transform of the image. However,

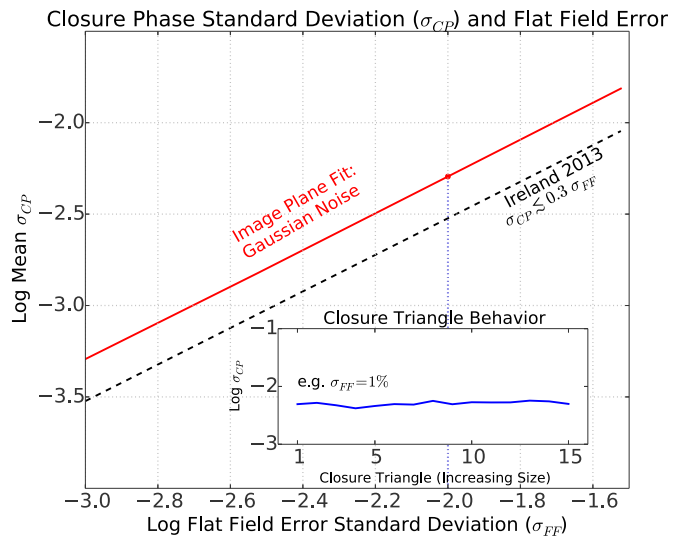


Figure 7. Flat field error (monochromatic): σ_{CP} , averaged over closure triangles, is compared to varying uncertainty in flat field, σ_{FF} . The solid red line shows our simulation results. The dotted black line displays a similar numerical result from Ireland (2013). Uncorrelated flat fielding error induces *baseline-independent* errors.

the intra-pixel sensitivity is not the same for all pixels, and/or is not symmetric, so is likely to contribute fringe phase error.

Uncharacterized IPS variations are prone to have a larger effect on coarsely sampled images than finely sampled ones. Figure 8 compares the effects of sampling frequency when IPS varies from pixel to pixel. We compare the sampling in NIRISS F277W and F430M bands, and GPI *H* and *K* bands as illustrative examples.

Here we assume that flat fields are known perfectly, so we use uniform and symmetric pixel-to-pixel weighting in our model (Figure 8(B)–left) and fit data with many realizations of IPS drawn from the model we describe above (e.g., Figure 8(B)–right). We renormalize the total pixel efficiency to maintain a constant net sensitivity of each pixel to avoid confounding flat-fielding error with IPS effects. Figure 9 shows increasing closure phase error for increased coarseness in pixel scale. Although NIRISS’ F277W suffers most from IPS variation, we can still achieve below 10^{-3} radians in closure phase error with the 5% uncertainty in IPS. Fine scale dithering (Koekemoer & Lindsay 2005) and careful individual pixel IPS calibration could mitigate our sensitivity to worse-than-Nyquist pixel scales. We note in passing that the NIRISS F277W filter presents an interesting science opportunity for faint companion imaging. F277W covers an H_2O absorption feature that could help constrain planet chemistry and dust grain models (Cushing et al. 2006; Stephens et al. 2009; Currie et al. 2013).

IPS modeling can also help determine fractional-pixel positioning of objects on the detector, by cross-correlating image data with analytically generated reference PSFs at different sub-pixel centerings (Greenbaum et al. 2013a).

5. PSF MAGNIFICATION AND SPECTRAL THROUGHPUT

Uncertainty in the coordinate scaling of the PSF affects our linear fit. Scaling errors could arise from hole size or central wavelength uncertainty. Coordinate scaling magnifies the PSF envelope and contributes errors, particularly to longer baselines. The PSF magnification in the data can be determined

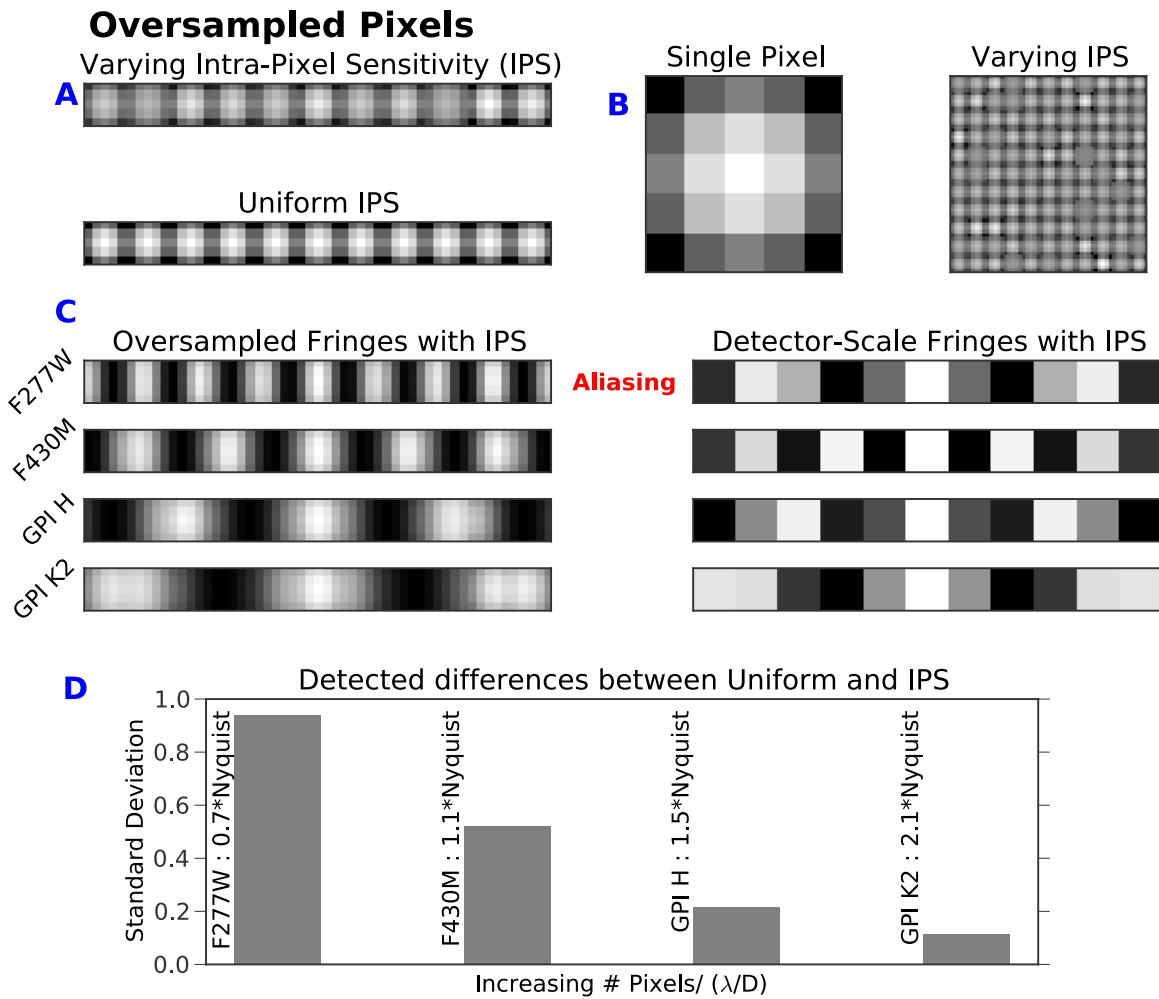


Figure 8. Intra-pixel sensitivity: a comparison between uniform IPS and pixel-to-pixel IPS variations (Hardy et al. 2008) on detectors with sub- and super-Nyquist pixellation. (A) Top left panel shows the sub-pixel sensitivity variation of two rows of 11 pixels, one with uniform IPS and the other with IPS realizations drawn from the statistical model. (B) A single pixel whose sensitivity drops quadratically to 80% at its corners, and an oversampled map of 11×11 pixels drawn from the statistical IPS model. (C) On the left, a finely sampled fringes ($5\times$ finer than the detector sampling) with varying IPS. On the right, the same response binned to the detector scale. At $2.77 \mu\text{m}$ the sampling is too coarse to detect the fringe peaks, which are aliased—only one peak is visible, though there are actually three. (D) The difference between image pixel counts for simulated detectors with uniform pixels and varying IPS. F430M (just Nyquist sampled) and F277W (about half Nyquist) show the largest errors. The two well-sampled GPI H and K2 bandpasses show much smaller errors. Figure 9 quantifies closure phase errors in these situations.

by cross-correlating the power spectrum of the data with power spectra of model PSFs created using a range of pupil scales. An NRM can be used to determine plate scale of IFS data cubes, thus providing an independent check of either plate scale or wavelength calibration in the hyperspectral data cubes (Greenbaum et al. 2013b).

Mask geometry or mask scale uncertainties will contribute errors in the closure phase when there are static pistons. Without static phase errors (i.e., with a symmetric PSF) there should be no error in closure phase. An asymmetric PSF (resulting from static piston error), however, will produce *baseline-dependent* closure phase errors, even when the model perfectly matches the data. We demonstrate that random static phases produce baseline-dependent closure phase error when fitting a polychromatic image, regardless of whether the model is monochromatic or polychromatic. Below about $\lambda/10$ waves (at the central wavelength) rms piston error the closure phase error scales with piston error. The effect is negligible when piston is below small fractions of a wave, when the PSF is sufficiently symmetric. In this section we use pistons that are uniformly distributed with an rms piston of 0.06 waves and zero mean (Table 2).

5.1. Hole Size Tolerance

The mask geometry must be known well to fit the diffractive image model to data. We simulate masks with seven identical holes. We used a Gaussian distribution of mask hole sizes with varied uncertainties and mean hole diameter d , the NRM hole size for NIRISS. Figure 10 compares hole size error σ_d to σ_{CP} . Contrast drops steeply with uncertainty in hole size in the presence of piston errors.

5.2. Fitting Medium- and Wide-band Data

NIRISS has three medium-band (5%–8% fractional bandwidth) filters intended for exoplanet science with NRM. Additionally, the wide-band F277W filter (25% fractional bandwidth) may also be scientifically interesting, despite its coarse sampling. Figure 11 demonstrates that a polychromatic model matches the data better than a monochromatic model, by about an order of magnitude. Closure phase errors for finite-bandwidth images with pistons are highly *baseline-dependent*. The errors vary by orders of magnitude between different closure triangles. Closure phase errors also depend on the shape of the bandpass for a given realization of piston errors, when fitting with a

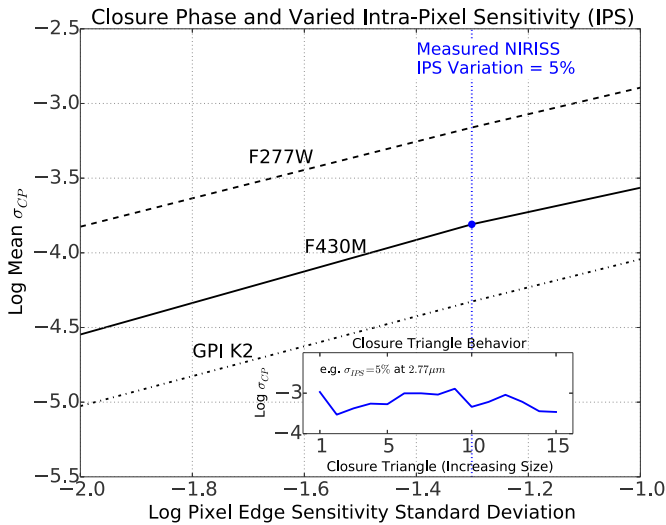


Figure 9. Varied intra-pixel sensitivity (monochromatic): closure phase errors resulting from a range of distributions of IPS. The relative edge sensitivity is varied, while maintaining a uniform net pixel quantum efficiency (see the text). NIRISS detector sampling at $2.77 \mu\text{m}$ and $4.3 \mu\text{m}$, and GPI sampling at K2 ($2.3 \mu\text{m}$) are shown.

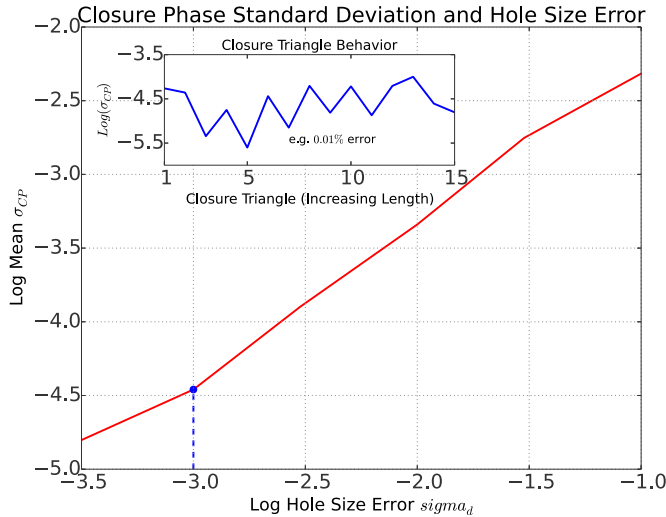


Figure 10. Hole size errors (monochromatic): we calculate σ_{CP} with a range of errors in hole diameter. Hole size only affects PSF envelope scaling, which is easily measured in the Fourier plane. Wavelength scales the entire PSF.

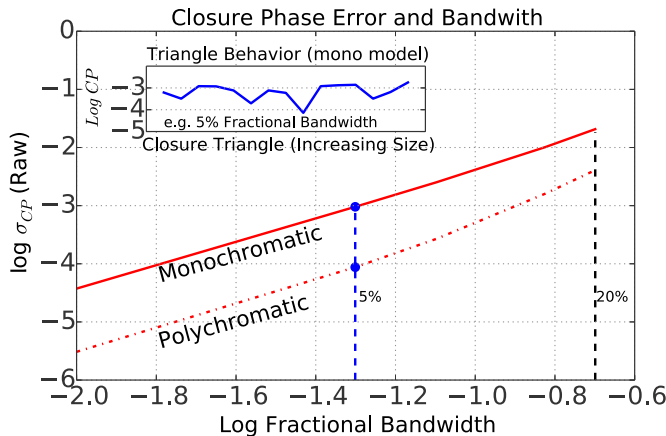


Figure 11. Fitting finite bandwidth data: Using a monochromatic model to fit finite bandwidth data achieves our required contrast only when the fractional bandwidth is $\lesssim 1\%$. Using a polychromatic model improves contrast by an order of magnitude. These closure phase errors are *baseline-dependent*, and are highly sensitive to the particular configuration of holes and pistons.

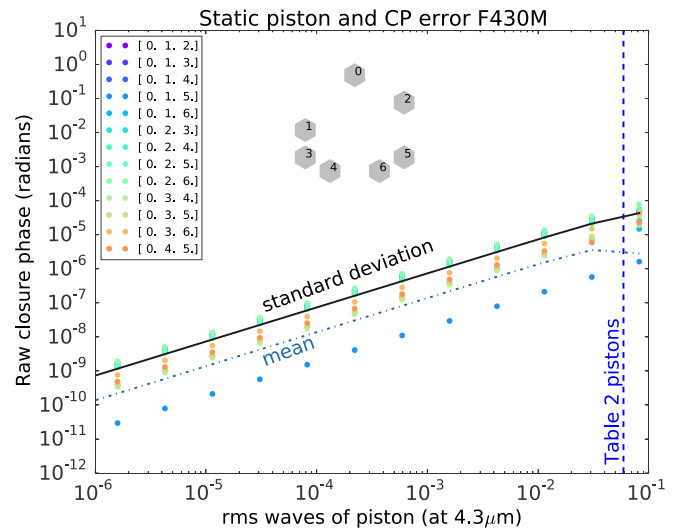


Figure 12. Spectrum errors and static piston in the pupil: we measure closure phase for polychromatic data with different levels of piston simulated with NIRISS's F430M filter and fit with a polychromatic model. The dependence is roughly linear when the pistons are below $\lambda/10$ at the central wavelength $\lambda_c = 4.3 \mu\text{m}$.

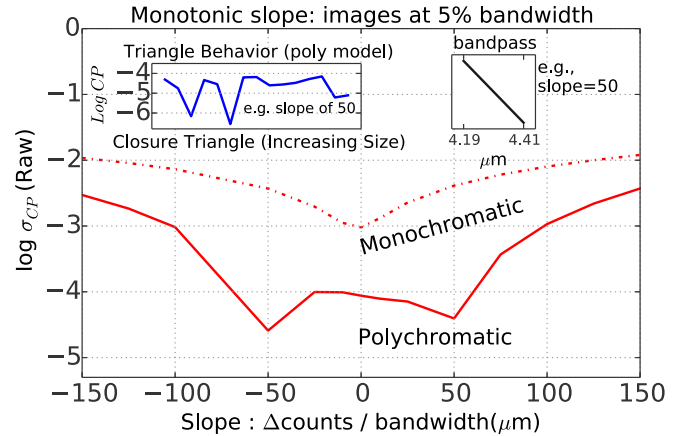


Figure 13. Bandpass shape: we fit noiseless polychromatic data generated with bandpasses of positive or negative slopes (difference in counts between the edges of the bandpass) with both a monochromatic model ($4.3 \mu\text{m}$), and a polychromatic model ($\lambda_c = 4.3 \mu\text{m}$) matching the bandpass. Surprisingly, the data are not fit best at zero slope with a polychromatic model. The shape of the bandpass can add small but significant errors because of averaging discussed in Section 3.5. Bandpass shape introduces *baseline-dependent* errors.

polychromatic model. Figure 11 suggests that mismatch in central wavelength can introduce large errors in closure phase.

Unless otherwise noted, we use the pistons described in Table 2 in these simulations. When there are no pistons in the pupil, error in the source spectrum should not contribute closure phase errors because the PSF remains symmetric. To explore how much piston affects closure phase error for polychromatic data fit with the model described in Equation (17), we simulated data with piston at small fractions of a wave and measured the resulting closure phase. The set of pistons in Table 2 were scaled uniformly to preserve the character of the errors while changing the size of the error. Closure phase error scales with the level of static piston up until an rms piston of about $\lambda/10$ (Figure 12).

Fitting polychromatic data with a polychromatic model will only introduce closure phase errors when there are non-zero pistons in the pupil and the PSF has asymmetries. The gross characteristics of the net throughput (filter \times source spectrum) sets a floor on raw contrast (Figure 13). This is likely because of

Effective stellar type mismatch - polychromatic model

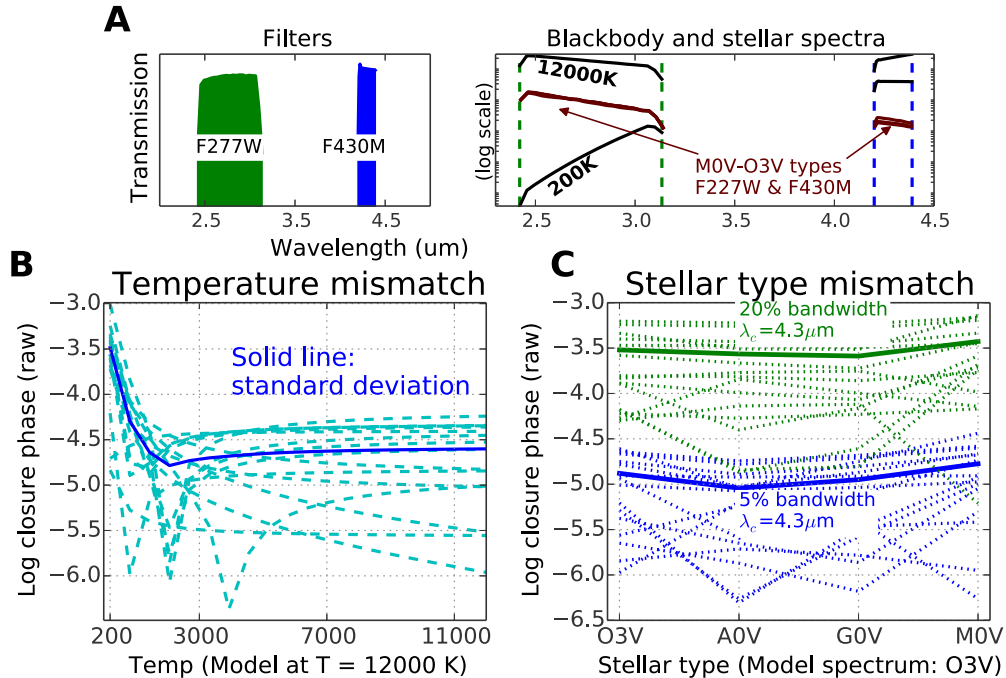


Figure 14. Spectrum error (polychromatic): (A) Left: transmission profiles for F430M and F277W NIRISS filters. Right: spectral profiles seen through the two NIRISS filters: blackbody spectra from $T_{\text{eff}} = 12,000$ K to $T_{\text{eff}} = 200$ K (subplot B) and stellar-type spectra (Castelli & Kurucz 2006) from M0V to O3V (subplot C). Large changes in spectral type do not strongly affect the slope of the spectrum. (B) The closure phase error (standard deviation over triangles in solid) plotted against blackbody temperature of simulated polychromatic data. The model temperature is $T_{\text{eff}} = 12,000$ K. Dashed lines represent individual closure triangles. (C) Closure phase is plotted against mismatch in stellar-type between the model created with an O3V stellar spectrum at a central wavelength $\lambda_c = 4.3 \mu\text{m}$ for 5% (blue) and 20% (green) bandwidths. Closure phases for all of 15 triangles are in dotted lines and their standard deviation in solid.

the piston averaging mentioned in Section 3.5. Polychromatic fitting is robust to smaller differences in throughput (e.g., slope) between the model and data.

JWST is anticipated to have 80% Strehl Ratio at $2 \mu\text{m}$. If its all wavefront error is in piston, piston standard deviation should be about 0.035 waves at $4.3 \mu\text{m}$. These values fall below $\lambda/10$ for the F430M filter. We assume that the filter is well known but the source spectrum is not. We investigate mismatch in blackbody spectrum (i.e., temperature) as well as an incorrect choice of stellar spectral type. We generate point source images for NIRISS F430M and F277W at a range of temperatures and stellar spectra, and fit each to either a $T = 12,000$ K blackbody or an O3V star model.

Figure 14(A) displays the F430M and F277W filter transmissions and range of blackbody curves, from our modeled spectrum at $T = 12,000$ K down to $T = 200$ K. Figure 14(B) displays raw closure phases for all of the 15 independent baselines and their standard deviation from fitting an incorrect blackbody model ($T = 12,000$ K) to data simulated at our range of temperatures. Similar to the bandpass shape simulation in Figure 13, there is an overall throughput shape that yields best sensitivity, though this behavior varies depending on baseline. The polychromatic image plane model is robust to a large error in blackbody temperature, up until the blackbody slope turns over for extremely cool objects (e.g., cooler than 670 K at $4.3 \mu\text{m}$).

We repeat the same procedure with a range of stellar photosphere models from Castelli & Kurucz (2006) to examine the effect of stellar type mismatch on closure phase sensitivity. Figure 14(A) shows that the range of stellar spectra from O3V to M0V stars in the two *JWST* filters do not differ much by slope. We model a flat bandpass centered at $\lambda_c = 4.3 \mu\text{m}$ at 5% and

20% to introduce the same rms piston. Figure 14(C) shows the raw closure phase error when the two models (using stellar type O3V) are fit to this range of spectra. The polychromatic image plane model shows similar robustness to poor knowledge of the stellar spectral type.

Polychromatic model fitting will not be a limiting factor on raw contrast for the narrowest filters with less than 0.06 waves rms piston, but becomes more of a concern for wide-band images, especially at shorter wavelengths. For small piston WFE, raw contrast for NRM with the F277W filter is not limited by the size of the bandpass compared to the effect of intrapixel sensitivity or flat field errors.

6. HIGHER SPATIAL FREQUENCY WAVEFRONT ERROR

Wavefront errors can introduce both amplitude and phase aberration in an image. NRM is most effective in the low spatial frequency wavefront error regime; closure phases are insensitive, to first and second order, to piston wavefront error (Ireland 2013). Wavefront errors on mirror segments often span a range of spatial frequencies. We used WebbPSF (Perrin et al. 2012) to simulate NIRISS NRM PSFs with low-to mid-spatial frequency wavefront errors, including segment tip and tilt, and figure errors on the segments and instrument optics.

We first explore the contribution of tip/tilt error by introducing randomly oriented tilts on simulated *JWST* mirrors. In Figure 15 each trial has a fixed tilt magnitude, which we place on 6 mirrors. We require a mean tilt of zero by constraining the last mirror so that we do not actually shift the centering of the PSF. Closure phase errors of 10^{-4} result from segment tilts of the order of half a resolution element.

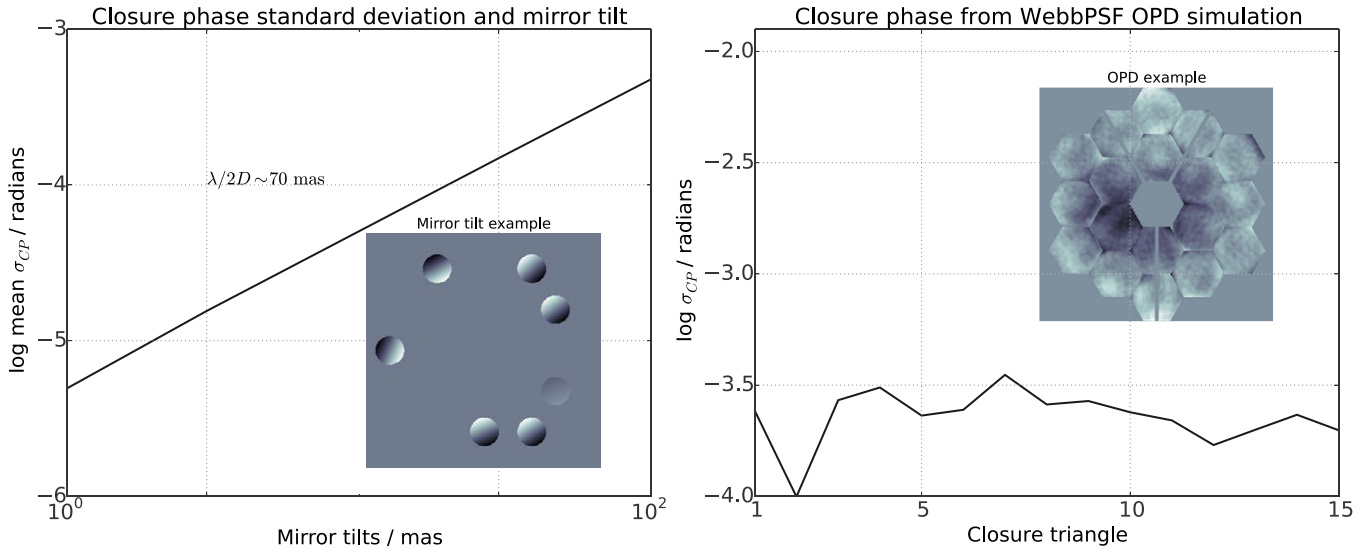


Figure 15. Tilts and higher order wavefront error: Top: we measure σ_{CP} from 100 different tilt error simulations of various sizes of tilt. An instance of tilt over each hole is inset in the top panel. Bottom: σ_{CP} from fitting 10 different ~ 140 nm rms *JWST* NIRISS wavefront realizations containing higher order wavefront error (Knight et al. 2012). PSFs were generated with WebbPSF software (Perrin et al. 2012).

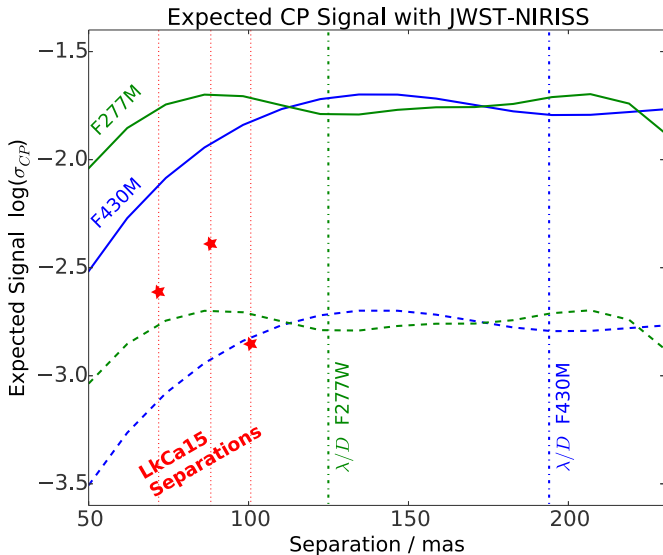


Figure 16. LkCa15 with *JWST* NIRISS: the theoretical closure phases for a single binary companion predict a required contrast $\approx 1/\sigma_{CP}$ empirically. The plot shows σ_{CP} over all possible triangles through NIRISS F277M and F430M filters. If F277M observations can reliably measure closure phase below 10^{-3} , they could detect the K' signal of the companion structure around LkCa15, according to Kraus & Ireland (2012). Two of their three companion sources lie between $\lambda/2D$ and λ/D at $2.77 \mu\text{m}$.

We also calculated closure phases for 10 different PSF realizations of ~ 140 nm rms optical path delay (OPD) on the *JWST* primary (Knight et al. 2012) using WebbPSF (Figure 15). These sample OPDs do not contain significant segment tilt or global focus. Fitting simulated data with this WFE yields $\sigma_{CP} = 10^{-3.5}$.

7. DETECTING THE COMPANION AROUND LkCa15 WITH *JWST* NIRISS

We consider the case of LkCa 15, which has a detected companion inside its disk gap, to compare simulated NIRISS NRM to current ground-based NRM. In Figure 16 we plot the theoretical binary closure phase signal for the mask on NIRISS

at $4.3 \mu\text{m}$ and $2.77 \mu\text{m}$ for two flux ratios: 10^{-2} and 10^{-3} . The red stars mark the Keck Telescope K' and L' detections of companion structure around LkCa15, a transitional disk with potential planet-forming bodies (Kraus & Ireland 2012). The LkCa15 detections fall between $0.5\lambda/D$ and λ/D for $2.77 \mu\text{m}$ (D referring to longest baseline), and are detectable with contrast better than 10^{-3} .

The F277W filter, at shorter wavelength, will access smaller inner working angles, relevant to following up close companions detected with large apertures on the ground. Following our analysis in Sections 4–6, we conclude that F277W would be able to achieve raw contrast of 10^{-3} with good flat field measurements and IPS characterization. With this performance NIRISS would be able to detect the LkCa15 companion signal in a routine observation.

At $2.77 \mu\text{m}$, $\lambda/2B \sim 88$ mas for NIRISS NRM. Detections this close to the diffraction limit may be challenging from a modeling perspective. The anticipated stability of NIRISS NRM's visibility amplitudes may help in breaking contrast-separation degeneracies more securely than in similar ground-based data. Multi-band observations may also help resolve degeneracies between separation and contrast. While the angular separation LkCa15's companions may still pose a challenge, NIRISS will likely achieve better contrast than ground-based NRM.

8. DISCUSSION AND RECOMMENDATIONS

Our analysis of the limits on raw contrast helps develop instrument tests, calibration needs, and observing strategies for *JWST* NIRISS. We applied our analytic model to NIRISS' cryogenic test data (Greenbaum et al. 2014). The necessary conditions for 10^{-4} closure phase error with NIRISS NRM depend strongly on detector behavior and other instrument and telescope details. Instrument characterization and accurate pointing and dithering, coupled with point source calibration of science target data could help achieve this contrast goal for routine NIRISS observations. Because of thermal drift and the planned occasional wavefront control activity in flight (Lightsey et al. 2004; Gardner et al. 2006; Makidon et al. 2008), near-contemporaneous acquisition of target and point

source calibrator data is desirable. Since NIRISS point source calibration involves system-wide complexities we defer study of it here. NRM paired with the sub-Nyquist sampled F277W filter should provide about 7.5 mag raw contrast, which could be useful for probing water absorption features.

Identifying outlying image pixels is straightforward with our analytical model fit. Our algorithm also makes for more efficient observing strategies since missing pixel data do not need to be filled in with dithered observations. Pixel-to-pixel variation in sub-pixel scale differences is easily incorporated in a statistical or detailed manner in our model fit approach, and saturated pixels can be ignored in the fit. This is relevant to NIRISS, with its barely-Nyquist pixel scale and *JWST*'s limited lifetime.

Flat field errors of 0.1% limit raw monochromatic contrast to a few $\times 10^{-4}$. Precise positioning of the target and calibrator on the same pixel will reduce the effect of flat field errors (Sivaramakrishnan et al. 2009b). Knowledge of intra-pixel sensitivity can be used to improve astrometry and reduce fringe phase measurement errors (Greenbaum et al. 2013a). Intra-pixel sensitivity (IPS) variations over the detector limit contrast, especially for the shorter wavelength NIRISS F277W and F380M filters. However, knowledge of the IPS can ameliorate this. We demonstrated that a statistical understanding of IPS variations can help markedly. As with flat field errors, repeated placement of targets to sub-pixel accuracy will benefit NIRISS NRM's contrast.

Small scaling errors may introduce closure phase errors when there are static piston in the pupil. Matching magnification between data and model is straightforward in the Fourier domain. For instruments that have IFSs, this technique can be used either for wavelength or for plate scale calibration of individual hyperspectral cube slices (Greenbaum et al. 2013b).

NIRISS NRM data analysis in the image plane will benefit from polychromatic modeling. The necessary piston averaging at the band's central wavelength will contribute closure phase errors when there are non-zero pistons in the pupil. However, the modeled bandpass is fairly robust to errors in source spectrum, as long as the spectrum slope sign is correct. Raw contrast from F277W observations will be reduced because of its wider bandpass, and because F277W will see higher instrument WFE at its shorter wavelength. However, with the anticipated WFE for *JWST*, its bandpass should not be the limiting factor for contrast.

The primary contrast limiting factors are pixel-to-pixel (flat field) variations and IPS variation for the coarsest sampled F277W filter. In comparison contrast will be largely unaffected by uncertainty in source spectrum if the modeled bandpass roughly matches the data. While these various systematics limit raw contrast, additional sensitivity will be possible through point-source calibrations and leveraging stable closure amplitudes.

Flat field errors can also effect closure phase measurements from IFS images. but higher order wavefront error from atmospheric effects may be the biggest limiting factor on the ground. These higher order errors certainly exist on ground-based instruments like GPI, and may contribute amplitude as well as phase errors. *JWST* NIRISS' wavefront error is expected to be dominated by low order terms, and stay below about 160 nm rms. Fitting uncorrelated pistons with our analytic model is robust to low-order wavefront errors including tip and tilt. A thorough study of the effects of higher-frequency wavefront error in the NRM PSF is warranted.

Table 3
Nominal NRM Hole Centers in *JWST*
Primary Mirror Space

Segment	V2 (mm)	V3 (mm)
C1	1143	1980
B2	2282	1317
C2	2286	0
B4	0	-2635
B5	2282	-1317
B6	2282	1317
C6	1143	1980

Space-based NRM presents opportunities for extended object imaging at high angular resolution. Centro-symmetric structures require amplitude measurements, which will be stable in the absence of atmospheric effects. Space-based NRM's fringe phase and amplitude measurements provide true imaging, which can benefit AGN and quasar science (Ford et al. 2014), so our image plane model could improve observing efficiency and data reduction methods for space-based high resolution imaging. An analytic point source model is a step towards more sophisticated forward-modeling of NRM data.

We acknowledge Ron Allen, Anthony Cheetham, Erin Eliot, Étienne Artigau, and Rémi Soummer for useful comments and both anonymous referees for insightful suggestions. This material is based upon work supported in part by the National Science Foundation Graduate Research Fellowship Program under grant No. DGE-1232825, by NASA grant APRA08-0117, and the STScI Director's Discretionary Research Fund.

APPENDIX

THE *JWST* NIRISS NON-REDUNDANT MASK

NIRISS's non-redundant mask design exposes the central parts of 7 of *JWST*'s segments in the outer ring of 12 segments. Table 3 defines the nominal, as-designed, mask in primary mirror space (shown in Figure 17). The mask's throughput is approximately 15% of the full aperture throughput (assuming spatially uniform primary mirror reflectivity). Thus the expected theoretical peak NRM PSF intensity is $1/(0.15)^2 = 44$ times fainter than the corresponding the full aperture PSF. In practice details of image centering, finite angular size of pixels, filter bandpass, source spectrum, and the intra-pixel sensitivity will cause slight deviations from this ratio. NIRISS's F380M, F430, and 480M filters provide sufficiently fine sampling on its 65 mas pixel scale detector. NIRISS is Nyquist sampled at $4 \mu\text{m}$. We have demonstrated reduced but still scientifically interesting capability for NIRISS's NRM when used with the wide band F277W filter as well.

Table 4 shows a rough comparison of the estimated thermal backgrounds assuming Keck-NIRC2's nine-hole mask and *JWST* NIRISS' seven-hole masks in many of the filters that are used with their NRMs. We assume that the ground-based mask itself is cooled, so does not contribute to the thermal background. Ground-based NRM is restricted to brighter adaptive optics guide stars, is limited by thermal background longward of $3 \mu\text{m}$, but delivers better angular resolution than NIRISS' NRM. On the other hand, *JWST* NIRISS' NRM extends to $4.8 \mu\text{m}$ with

Table 4
Estimated Thermal Background Rates for a Ground-based 10 m Telescope (left) and *JWST* NIRISS (right)

Wavelength (μm)	Bandwidth (%)	Background ($e^- \text{s}^{-1} \text{pixel}^{-1}$)	Wavelength (μm)	Bandwidth (%)	Background ($e^- \text{s}^{-1} \text{pixel}^{-1}$)
1.65	20	5×10^{-4}	2.77	25	0
2.20	20	6×10^{-1}	3.80	5	9×10^{-2}
3.50	20	1×10^3	4.30	5	4×10^{-1}
4.30	20	1×10^4	4.80	8	5×10^{-1}

Notes. This rough estimate uses typical operating temperatures (273 K for a ground-based telescope and 50 K for *JWST* and NIRISS, and assumes that the thermal background for the ground-based telescope is entirely due to warm mirrors. On *JWST* NIRISS the entire opaque mask area will be the dominant source of thermal background. We use an emissivity of 0.1 for the warm Keck mirrors, and a system efficiency of 0.5 for both cases.

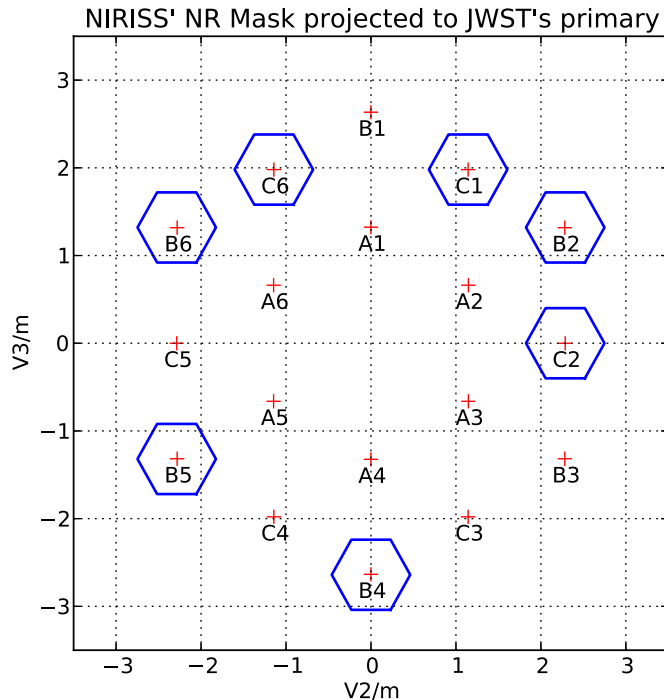


Figure 17. Layout of the seven-hole NIRISS NRM mask in *JWST* primary mirror coordinates (after Sivaramakrishnan et al. 2009b). The (V_2 , V_3) axes are in the plane of the *JWST* pupil. A viewer located at the secondary mirror and looking at the reflective surface of the primary mirror would see this mask projection and segment arrangement. The centers of the 18 segments (designated A1-6, B1-6, and C1-6) are labeled. The NRM's holes are nominally centered on the segment they expose. The holes are 0.8 m flat-to-flat when projected back to the primary mirror. The average segment flat-to-flat distance is approximately 1.32 m if there were no inter-segment gaps. The mask's holes are undersized so as to stay within the parent segment in the presence of a linear pupil misalignment of up to 3.8% of the diameter of the pupil's circumscribing circle, *viz.*, 6603.5 mm at operating temperature (P. Lightsey 2011, private communication; M. Beaulieu 2011, private communication). All these numbers will need to be refined when the as-built pupil distortion is measured on the ground and in flight.

no appreciable thermal background, so it should be able to observe much fainter targets than are available to instruments such as Keck-NIRC2 NRM. We note that thermal background limits Keck-NIRC2's L' and M_s filters to exposures of the order of 0.27 and 0.14 s respectively.

REFERENCES

Baldwin, J. E., Haniff, C. A., Mackay, C. D., & Warner, P. J. 1986, *Natur*, 320, 595
 Beichman, C. A., Krist, J., Trauger, J. T., et al. 2010, *PASP*, 122, 162
 Bernat, D., Bouchez, A. H., Ireland, M., et al. 2010, *ApJ*, 715, 724

Beuzit, J.-L., Feldt, M., Dohlen, K., et al. 2008, *Proc. SPIE*, 7014, 701418
 Biller, B. A., Liu, M. C., Wahhaj, Z., et al. 2013, *ApJ*, 777, 160
 Bos, B. J., Kubalak, D. A., Antonille, S. R., et al. 2008, *Proc. SPIE*, 7010, 70103C
 Castelli, F., & Kurucz, R. L. 2006, *yCat*, 345, 40333
 Cheetham, A. C., Tuthill, P. G., Sivaramakrishnan, A., & Lloyd, J. P. 2012, *OExpr*, 20, 29457
 Cieza, L. A., Lacour, S., Schreiber, M. R., et al. 2013, *ApJL*, 762, L12
 Currie, T., Burrows, A., Madhusudhan, N., et al. 2013, *ApJ*, 776, 15
 Cushing, M. C., Roellig, T. L., Marley, M. S., et al. 2006, *ApJ*, 648, 614
 Doyon, R., Hutchings, J. B., Beaulieu, M., et al. 2012, *Proc. SPIE*, 8442, 84422R
 Ford, K. E. S., McKernan, B., Sivaramakrishnan, A., et al. 2014, *ApJ*, 783, 73
 Gardner, J. P., Mather, J. C., Clampin, M., et al. 2006, *SSRv*, 123, 485
 Girard, J. 2013, NACO User Manual, European Southern Observatory, VLT-MAN-ESO-14200-2761 (available online at http://www.eso.org/sci/facilities/paranal/instruments/naco/doc/VLT-MAN-ESO-14200-2761_v82.pdf)
 Greenbaum, A. Z., Martel, A., Sivaramakrishnan, A., et al. 2014, *Proc. SPIE*, 9143, 91434M
 Greenbaum, A. Z., Sivaramakrishnan, S., & Pueyo, L. 2013a, *Proc. SPIE*, 8864, 88641L
 Greenbaum, A. Z., Sivaramakrishnan, S., Pueyo, L., et al. 2013b, *Proc. SPIE*, 8864, 88641V
 Haniff, C. A., Mackay, C. D., Titterton, D. J., Sivia, D., & Baldwin, J. E. 1987, *Natur*, 328, 694
 Hardy, T., Baril, M. R., Pazder, J., & Stilburn, J. S. 2008, *Proc. SPIE*, 7021, 70212B
 Hinkley, S., Carpenter, J. M., Ireland, M. J., & Kraus, A. L. 2011, *ApJL*, 730, L21
 Huélamo, N., Lacour, S., Tuthill, P., et al. 2011, *A&A*, 528, L7
 Ireland, M. J. 2013, *MNRAS*, 433, 1718
 Ireland, M. J., Kraus, A., Martinache, F., Law, N., & Hillenbrand, L. A. 2011, *ApJ*, 726, 113
 Ireland, M. J., Kraus, A., Martinache, F., Lloyd, J. P., & Tuthill, P. G. 2008, *ApJ*, 678, 463
 Knight, J. S., Acton, D. S., Lightsey, P., & Barto, A. 2012, *Proc. SPIE*, 8449, 84490V
 Koekemoer, A. M., & Lindsay, K. 2005, STScI Instrument Science Report ISR-TEL-2005-03 (Baltimore, MD: STScI)
 Kraus, A. L., & Ireland, M. J. 2012, *ApJ*, 745, 5
 Lacour, S., Tuthill, P., Amico, P., et al. 2011, *A&A*, 532, A72
 Lauer, T. R. 1999, *PASP*, 111, 1434
 Lightsey, P. A., Barto, A. A., & Contreras, J. 2004, *Proc. SPIE*, 5487, 825
 Lloyd, J. P., Martinache, F., Ireland, M. J., et al. 2006, *ApJL*, 650, L131
 Macintosh, B., Graham, J. R., Ingraham, P., et al. 2014, *PNAS*, 111, 12661
 Macintosh, B. A., Anthony, A., Atwood, J., et al. 2012, *Proc. SPIE*, 8446, 84461U
 Makidon, R. B., Sivaramakrishnan, A., Soummer, R., Anderson, J., & van der Marel, R. P. 2008, *Proc. SPIE*, 7010, 701000
 Martinache, F. 2010, *ApJ*, 724, 464
 Martinache, F. 2011, *Proc. SPIE*, 8151, 815111
 Martinache, F., & Guyon, O. 2009, *Proc. SPIE*, 7440, 744000
 Martinache, F., Lloyd, J. P., Ireland, M. J., Yamada, R. S., & Tuthill, P. G. 2007, *ApJ*, 661, 496
 Martinache, F., Rojas-Ayala, B., Ireland, M. J., Lloyd, J. P., & Tuthill, P. G. 2009, *ApJ*, 695, 1183
 Metchev, S. A., & Hillenbrand, L. A. 2004, *ApJ*, 617, 1330
 Monnier, J. D. 2003, *RPPH*, 66, 789
 Nielsen, E. L., Liu, M. C., Wahhaj, Z., et al. 2013, *ApJ*, 776, 4

- Oppenheimer, B. R., Beichman, C., Brenner, D., et al. 2012, *Proc. SPIE*, 8447, 844720
- Perrin, M. D., Soummer, R., Elliott, E. M., Lallo, M. D., & Sivaramakrishnan, A. 2012, *Proc. SPIE*, 8442, 84423D
- Pope, B., Martinache, F., & Tuthill, P. 2013, *ApJ*, 767, 110
- Readhead, A. C. S., Nakajima, T. S., Pearson, T. J., et al. 1988, *AJ*, 95, 1278
- Sabatke, E., Burge, J., & Sabatke, D. 2005, *ApOpt*, 44, 1360
- Sivaramakrishnan, A., Lafrenière, D., Ford, K. E. S., et al. 2012, *Proc. SPIE*, 8442, 84422S
- Sivaramakrishnan, A., Lafrenière, D., Tuthill, P. G., et al. 2010a, *Proc. SPIE*, 7731, 77313W
- Sivaramakrishnan, A., Soummer, R., Oppenheimer, B. R., et al. 2010b, *Proc. SPIE*, 7735, 773586
- Sivaramakrishnan, A., Tuthill, P., Martinache, F., et al. 2009a, *Astro2010: The Astronomy and Astrophysics Decadal Survey*, No. 40 (arXiv:0904.1360)
- Sivaramakrishnan, A., Tuthill, P. G., Ireland, M. J., et al. 2009b, *Proc. SPIE*, 7440, 74400Y
- Stephens, D. C., Leggett, S. K., Cushing, M. C., et al. 2009, *ApJ*, 702, 154
- Teague, M. R. 1982, *JOSA*, 72, 1199
- Thompson, A. R., Moran, J. M., & Swenson, G. W. 1986, *Interferometry and Synthesis in Radio Astronomy* (New York: Wiley)
- Troy, M., & Chanan, G. 2003, *ApOpt*, 42, 3745
- Tuthill, P. G., Monnier, J. D., Danchi, W. C., Wishnow, E. H., & Haniff, C. A. 2000, *PASP*, 112, 555
- Vigan, A., Patience, J., Marois, C., et al. 2012, *A&A*, 544, A9
- Wahhaj, Z., Liu, M. C., Nielsen, E. L., et al. 2013, *ApJ*, 773, 179
- Zimmerman, N., Sivaramakrishnan, A., Bernat, D., et al. 2012, *Proc. SPIE*, 8445, 84452G
- Zimmerman, N. T. 2011, PhD thesis, Columbia University